1   **Distinct upper airway epithelium interferon-stimulated and profibrotic gene expression**

2   **between adult and infant rhesus macaques infected with SARS-CoV-2**

3

4   Stephanie N. Langel[1], Carolina Garrido[2], Caroline Phan[2], Tatianna Travieso[2], Todd DeMarco[2],

5   Zhong-Min Ma[3], Rachel Reader[3], Katherine J. Olstad[3], Rebecca L. Sammak[3], Yashavanth

6   Shaan Lakshmanappa[4], Jamin W. Roh[4,5], Jennifer Watanabe[3], Jodie Usachenko[3], Ramya

7   Immareddy[3], Rachel Pollard[4], Smita S. Iyer[3,4,6], Sallie Permar[7], Lisa A. Miller[3,8], Koen K.A. Van

8   Rompay[3] and Maria Blasi[2,9*]

9

10   [1] Duke Center for Human Systems Immunology and Department of Surgery, Duke University

11   School of Medicine, Durham, NC, USA

12   [2] Duke Human Vaccine Institute, Duke University School of Medicine, Durham, NC, USA

13   [3] California National Primate Research Center, University of California, Davis, CA USA

14   [4] Center for Immunology and Infectious Diseases, University of California, Davis, CA USA

15   [5] Graduate Group in Immunology, UC Davis, CA

16   [6] Department of Pathology, Microbiology, and Immunology, School of Veterinary Medicine, UC

17   Davis, CA

18   [7] New York-Presbyterian/Weill Cornell Medical Center, Department of Pediatrics, New York, NY,

19   USA

20   [8] Department of Anatomy, Physiology, and Cell Biology, School of Veterinary Medicine, UC

21   Davis, CA

22   [9] Department of Medicine Division of Infectious Diseases, Duke University School of Medicine,

23   Durham, NC, USA

24
25   #Address correspondence to: Maria Blasi, Duke University Medical Center, 2 Genome Ct,
26   27710 Durham, NC, USA. Email: maria.blasi@duke.edu.

27 **Abstract**

28 The global spread of Severe Acute Respiratory Syndrome Coronavirus 2 (SARS-CoV-2) and its

29 associated coronavirus disease (COVID-19) has led to a pandemic of unprecedented scale. An

30 intriguing feature of the infection is the minimal disease in most children, a demographic at

31 higher risk for respiratory viral diseases. To elucidate age-dependent effects of SARS-CoV-2

32 pathogenesis, we inoculated two rhesus macaque monkey dam-infant pairs with SARS-CoV-2

33 and conducted virological and transcriptomic analysis of the respiratory tract and evaluated

34 systemic cytokine and antibody responses. Viral RNA levels in all sampled mucosal secretions

35 were comparable across dam-infant pairs in the respiratory tract. Despite comparable viral

36 loads, adult macaques showed higher IL-6 in serum while CXCL10 was induced in all animals.

37 Both groups mounted neutralizing antibody (nAb) responses, with infants showing a more rapid

38 induction at day 7. Transcriptome analysis of tracheal tissue isolated at day 14 post-infection

39 revealed significant upregulation of multiple interferon-stimulated genes in infants compared to

40 adults. In contrast, a profibrotic transcriptomic signature with genes associated with cilia

41 structure and function, extracellular matrix (ECM) composition and metabolism, coagulation,

42 angiogenesis, and hypoxia was induced in adults compared to infants. Our observations

43 suggest age-dependent differential airway responses to SARS-CoV-2 infection that could

44 explain the distinction in pathogenesis between infants and adults.

45

46 **Introduction**

47 The epidemiological evidence has consistently demonstrated that SARS-CoV-2 infections in

48 young children are mostly mild with relatively low hospitalization rates (1, 2). This results in

49 significantly decreased fatality rates of young (0-9 years old) compared with old (>70-year-old)

50 populations (3-9). Despite the increase in pediatric hospitalizations during emergence of the

51 Delta variant, the proportion of children with severe disease after the Delta variant became

52 predominant were similar to those earlier in the pandemic (10). This suggests that the increase

53 in pediatric hospitalizations during this time is related to other factors, and that children are still

54 at significantly lower risk to severe COVID-19 compared to adults.

55 Differences in local immune responses in the respiratory tract that include antiviral and pro-

56 inflammatory mediators likely play a role in the age-dependent pathogenesis of SARS-CoV-2

57 (11). A recent study showed that children have increased expression of relevant pattern

58 recognition receptors including MDA5 (*IFIH1*) and RIG-I (*DDX58*) in the upper airways when

59 compared to adults, suggesting that recognition of SARS-CoV-2 entry into respiratory cells is

60 enhanced in children (12). This is relevant for recruitment of fast-acting innate immune cells like

61 neutrophils, which were shown to be higher in children during the acute phase of SARS-CoV-2

62 infection compared to adults (13). Interferon (IFN) responses are also key determinants of

63 COVID-19 severity, and potent production of type III, and to a lesser extent type I IFNs in the

64 upper respiratory tract are associated with decreased viral load, milder COVID-19 and younger

65 age (14). However, there remains a large gap in our understanding of how age-dependent

66 factors mediate disease severity and recovery post-infection.

67 Non-human primate (NHP) models are valuable resources to address these questions related to

68 SARS-CoV-2 pathobiology and to explore vaccine and drug-based interventions against

69 COVID-19 (15, 16). In this pilot study, we developed a maternal-infant SARS-CoV-2 infection

70 model to elucidate the age-dependent effects on viral pathogenesis. By using dam-infant pairs

71 and inoculating both dam and infant at the same time, we were able to simultaneously analyze

72   immune responses to SARS-CoV-2 infection in two different age groups while limiting genetic

73   variation. We show that SARS-CoV-2 infection in dam-infant rhesus macaque pairs results in

74   innate and adaptive immune differences including SARS-CoV-2 neutralizing antibody response

75   kinetics and innate immune and profibrotic gene expression in the conducting airways. Our data

76   highlight age-dependent differential immune and lung responses to SARS-CoV-2 infection that

77   may be important to guide the prevention and treatment of severe COVID-19.

78

79   **Results**

80   **Experimental design and SARS-CoV-2 infection of dam/infant pairs**

81   To investigate age-dependent differences in pathogenesis of SARS-CoV-2, two dams and their

82   6-month-old infants were inoculated intranasally and intratracheally with SARS-CoV-2 (USA-

83   WA1/2020 isolate). Nasal and pharyngeal swabs, bronchoalveolar lavage (BAL), blood, breast

84   milk and rectal swabs were collected over time up to day 14 post-challenge (**Fig. 1A**).

85   To compare viral replication kinetics between the adult dams and infant macaques after SARS-

86   CoV-2 infection, we performed both genomic (Orf1a gene) and subgenomic (N gene) PCR on

87   nasal (dams only), pharyngeal, buccal and rectal swabs. Nasal swabs were not collected from

88   infants due to restricted size of infant nostrils. As shown in **Fig. 1B,C**, we did not detect

89   significant differences in viral loads between adults and infants in pharyngeal or BAL

90   supernatant or BAL pellet (**Supplemental Fig. 1**) samples. Low levels of viral RNA were

91   detected in one of the two infants in buccal and rectal swabs, while no viral RNA was detected

92   in breast milk (**Supplemental Fig. 1**).

93   We evaluated clinical symptoms and radiographic changes overtime. Mild symptoms, including

94   occasional sneezing were reported. The radiographs were scored for the presence of

95   pulmonary infiltrates, according to a standard scoring system (0 to 3 per lobe). Individual lobes

96   were scored and scores per animal per day were totaled. Only the adult macaques had scores

97   on multiple (≥2) days and the highest scores observed (score of 5) were from one of the adult

98   macaques (**Supplementary Table 1**). Overall in both age groups the lesions in the lung were

99   minimal and largely resolved consisting of occasional foci of mild inflammation on HE stained

100   sections (**Supplemental Fig. 2**). Trichrome stained sections did not show an overt increase in

101   fibrosis in either group. There was no significant evidence of interstitial pneumonia in any

102   animal, only occasional focal increase in interstitial cellularity and in some areas an increase in

103   alveolar macrophages, as previously reported (17).

104   **Systemic innate cellular and cytokine responses in SARS-CoV-2-infected dam and infant**

105   **rhesus macaques**

106   We evaluated innate immune cell subsets in the peripheral blood and observed no major

107   differences in proportion of cells between infant and dams after SARS-CoV-2 infection (**Fig.**

108   **2A**). Interestingly, however circulating neutrophils (lineage-, CD66+) and total HLA-DR+

109   (lineage-, CD66-) cells, comprising of monocytes and dendritic cell subsets, were higher in

110   adults and infants prior to inoculation with SARS-CoV-2, respectively (**Fig. 2A**). For plasma

111   cytokine responses, we observed greater than a 2-fold increase in IL-6 (all 4 animals) and IP10

112   (CXCL10) (2 dams, 1 infant) as reported previously (18), and the anti-inflammatory mediator IL-

113   1RA (1 dam, 2 infants) within 1-day post SARS-CoV-2 infection (**Fig. 2B**). One infant

114   demonstrated increased production of IL-17 and GM-CSF at several time points post-infection.

115   Interestingly, IL-8 was upregulated greater than 7-fold in 3 of the 4 animals at day 14 post-

116   infection. However, we did not identify any specific cytokine signature that distinguished dams

117   from infants.

118   **Kinetics of neutralizing antibody (nAb) development differ between dam and infant**

119   **rhesus macaques infected with SARS-CoV-2**

120   We next measured anti-spike (S) binding and nAbs in serum and breast milk samples. With the

121   limitation that the small group sizes preclude statistical significance, we found that while dams

122   had higher serum S-binding IgG antibody titers than infants (**Fig. 3A**), infants demonstrated

123   faster kinetics of nAb development. Infants had higher nAb titers at day 7 post-infection, yet

124   similar nAb titers at day 14 post-infection compared to dams (**Fig. 3B)**. S-binding IgG, but not

125   IgA, was detected in breast milk of infected dams at day 14 post-infection (**Fig. 3C**). NAbs in

126   breast milk were detected in one dam at day 14 post-infection (**Fig. 3D**). A multiplexed antibody

127   binding assay did not detect differences in receptor binding domain (RBD), S1, S2, full S and N-

128   terminal domain (NTD)-specific antibodies between SARS-CoV-2-infected dam and infant

129   macaques at day 14 (**Fig. 3E**).

130   **Age-dependent differences in transcriptomic responses in the trachea reveal**

131   **downregulated interferon stimulated genes and cilia injury signatures in adult macaques**

132   The hierarchical and principal component analyses and heatmap (**Supplementary Fig. 3A-C**)

133   of the differentially expressed genes (DEGs) of tracheal cells (epithelial, immune and

134   mesenchymal) demonstrated altered transcriptomic expression of infant and dam rhesus

135   macaques on day 14 after SARS-CoV-2 infection, where mothers and offspring clustered with

136   each other (**Supplementary Fig. 3C**). To identify gene ontology (GO) and hallmark gene sets

137   associated with altered expression, gene set enrichment analysis (GSEA) was performed (1).

138   The Hallmark pathway analysis revealed a decrease in trachea cell genes associated with the

139   *Interferon Alpha* and *Interferon Gamma* Hallmark pathways in adult compared to infant

140   macaques (**Supplementary Table 2A**). Specifically, *IFI6*, *XAF1*, *DDX60*, *OAS2*, *HERC6*, *MX2*,

141   *IFI44L, IFIT1, SAMD9L, PARP14 and IFIT12* are significantly decreased in both adults

142   compared to their infants (**Fig. 4A, Supplementary Fig. 4**).

143   Alternatively, in the GO pathway analysis we identified an overwhelming signature of decreased

144   cilia structure and function in adult compared to infant tracheas (**Fig. 4B, Supplementary Fig.**

145   **5**). In fact, all GO pathways that were significantly enriched among downregulated genes

146   (FWER adjusted P-value ≤ 0.05) were related to cilia structure and motility (**Supplementary**

147 **Table 2B**). Considering SARS-CoV-2 infection induces a de-differentiation of multiciliated cells

148 (19), these results suggest a prolonged impairment of cilia functions in adult compared to infant

149 rhesus macaques 14 days after SARS-CoV-2 infection.

150 **Conducting airways of SARS-CoV-2 infected adult macaques show a profibrotic**

151 **transcriptomic signature**

152 In both the GO and Hallmark pathway analyses, there was significant enrichment among

153 upregulated genes (FWER adjusted P-value ≤ 0.05) for pathways associated with wound repair

154 and fibrosis in adult compared with infant macaques at day 14 post infection (**Supplementary**

155 **Table 3**). Of the forty GO pathways that are significantly enriched among upregulated genes in

156 the adult macaques, the overwhelming majority were associated with extracellular matrix (ECM)

157 organization and ECM metabolism (**Supplementary Table 3**). Similarly, the Hallmark pathway

158 analysis revealed multiple pathways associated with wound repair and fibrosis in adult

159 macaques including *Epithelial mesenchymal transition, Angiogenesis, Coagulation, Hypoxia,*

160 *Apoptosis and TGF beta signaling* (**Supplementary Table 4**). Of the most DEGs of the

161 upregulated pathways in adults compared to infants, all of them were associated with the ECM

162 (**Fig. 5A, Supplementary Fig. 7**). We stained trachea tissue for protein gene product 9.5 (PGP

163 9.5) (also known as ubiquitin C-terminal hydrolase-L1 [UCH-L1]) (**Fig. 5D-G**) and Substance P

164 (Sub P) (**Fig. 5 H-K**), proteins involved in wound healing (20, 21), which were both higher in

165 infant compared to adult tracheas (**Fig. 5**).

166

167 **Discussion**

168 In this pilot study, we evaluated age-dependent differences in SARS-CoV-2

169 pathogenesis by inoculating two dam-infant rhesus macaque pairs with SARS-CoV-2. We

170 demonstrate that both infant and dam rhesus macaques became productively infected and

171 exhibited no to mild clinical symptoms. These clinical observations are similar to those observed

172 in other NHP studies of SARS-CoV-2 infection in adults (15, 16). Lung radiograph scores

173   showed mild pulmonary infiltrates in both dams and infants, however only in dams were

174   pulmonary infiltrates observed for multiple days (≥2). Histologic examination of pulmonary

175   infiltrates was extremely minimal and largely resolving when examined day 14 post-infection.

176   This is consistent with previous experiments (18).

177   While viral loads in pharyngeal swabs and BAL samples did not differ between dam and

178   infant macaques, differences in antibody response kinetics between the dams and infants were

179   observed. For example, while there were higher anti-spike IgG binding antibody titers in adult

180   macaques at day 10 and 14 post-infection, infants exhibited higher nAb titers at day 7. These

181   data suggest faster kinetics of SARS-CoV-2 nAb responses in infant macaques. In pediatric

182   cohorts infected with SARS-CoV-2, results have been variable and levels of nAbs have been

183   reported as lower, higher or not different compared to infected adults (22-26). However, age-

184   dependent differences in nAb development have been observed for other pathogens. For

185   example, in HIV-1 infected children, circulating broadly neutralizing antibodies (bnAbs) arise

186   earlier in infection, and have higher potency and breadth compared to adults (27-32). Future

187   work using this model should include measurement of T cell subsets in both blood and lymphoid

188   tissue as well as determination of breadth against multiple SARS-CoV-2 variants.

189   Although there were not major differences in serum cytokines between adult and infant

190   SARS-CoV-2 infected macaques, we observed increases in relevant pro-inflammatory

191   cytokines. For example, IL-6 and IP10 (CXCL10) were increased in 3 of the 4 animals within 1-

192   day post SARS-CoV-2, mirroring what was previously reported in rhesus macaques and other

193   animal models of SARS-CoV-2 infection (33-35). In humans, IL-6 and IL-RA correlate with

194   COVID-19 severity (36, 37) while CXCL10 correlates with viral load in nasopharynx (38).

195   Interestingly, we observed a delayed increase in IL-8 in 3 of the 4 macaques at day 14 post-

196   infection. Following SARS-CoV-2 infected macaques for greater than 14 days would be

197   worthwhile in determining if late-onset pro-inflammatory signatures exist. Additionally,

198 measuring cytokines in tissues would give additional insight into age-dependent local responses

199 to infection.

200   There were not major differences in innate immune cell subsets between adult and infant

201 macaques in response to SARS-CoV-2 infection. While neutrophils were higher in adult

202 circulation prior to infection, this could be due to a stress-induced response (39). Interestingly,

203 HLA-DR+ (lineage-, CD66+) innate immune cells were higher in infant circulation prior to

204 infection compared to adults. Recent studies have observed differences in circulating subsets of

205 monocytes and dendritic cells during SARS-CoV-2 infection between children and adult cohorts

206 (13). Assessing cellular immune subsets in tissues will be an important next step to determine

207 age-dependent cellular trafficking after SARS-CoV-2 infection.

208   An increase in interferon alpha and gamma transcriptomic signatures were observed in

209 infant macaques compared to dams. There were multiple ISGs that were upregulated in both

210 infants compared to their dams, nearly all of which were previously shown to be significantly

211 upregulated after SARS-CoV-2 infection. Similarly, in a pediatric cohort of SARS-CoV-2-infected

212 children, there were multiple ISGs in epithelial cells of the upper respiratory tract that were

213 significantly increased compared to SARS-CoV-2-infected adults late during both the early (day

214 0-4) and late (day 5-12) phase of infection including *IRF3, TLR3, DHX58, IFIH1,* and *DDX58*

215 (12). Considering trachea RNA-seq data was collected at day 14 post-inoculation in our study,

216 when viral loads were not detectable anymore, it is possible that levels of some ISGs are

217 upregulated in infants at baseline compared to adults. Indeed, this has been demonstrated in

218 multiple pediatric cohorts where ISGs (40) and cytokines and chemokine genes (41) were

219 increased in SARS-CoV-2-uninfected children compared to adults. Upon SARS-CoV-2 infection,

220 children's IFN-α responses were greater in multiple immune cell subsets including NK CD56^{low},

221 NKT cells, neutrophils, CXCL10+ monocytes and some CD8+ T cell subsets (40). These data

222 suggest the IFN response in children is pre-activated in epithelial cells of the upper airways and

223 stronger in immune cell subsets compared to adults. An increase in innate immune effectors in

224   infants and children may also be explained by 'trained immunity'. Trained immunity results in

225   functional reprogramming of innate immune cells which leads to heterologous protection against

226   secondary infections (42). Considering children are infected more frequently and with a greater

227   number of viruses, it is possible that this leads to an induction of non-specific antiviral effects

228   (43, 44).

229   There was an overwhelming signature of decreased cilia structure and function-related

230   genes in adult compared to infant macaques. It has been previously demonstrated that SARS-

231   CoV-2 infection leads to dedifferentiation of multiciliated cells in vitro and in vivo (19).

232   Considering trachea RNA-seq data was collected at day 14 post-inoculation in our study, a time

233   when viral replication at mucosal sites was undetectable, it is possible that SARS-CoV-2-

234   infected adults have delayed cilia repair. Indeed, other groups have observed delayed repair

235   responses after pulmonary injury in adults. For example, hypoxia or LPS-induced lung injury

236   resulted in less lung inflammation and apoptosis in neonatal compared to adult mice, which was

237   dependent on increased NF-κβ activation (45, 46). Additionally, neonatal mice had reduced lung

238   permeability and pulmonary barrier disruption compared to adult mice after LPS administration,

239   despite similar degrees of inflammation and cellular apoptosis (47). These data and our results

240   support the hypothesis that the impacts of SARS-CoV-2 infection in the airways, including

241   inflammation, apoptosis and barrier permeability (that implicates cilia structure and function), are

242   lessened in neonates and young children compared to adults.

243   We observed that multiple genes and pathways associated with ECM composition and

244   metabolism, coagulation, angiogenesis and hypoxia are increased in the trachea of dams

245   compared to infants. These profibrotic transcriptomic signatures suggest greater activation of

246   the cellular repair process in response to injury and apoptosis in the upper airway in adults

247   compared to infants. Indeed, the deposition of multiple components of the lung ECM including

248   hyaluronan and fibrinogen (48-50) as well as profibrotic macrophage accumulation (50) has

249   been associated with severe COVID-19 in adults. Additionally, an increase in ECM-remodeling

250   enzymes is associated with lethal immunopathology during severe influenza infection (51).

251   Alterations in ECM can be not only a consequence of lung fibrosis but also a driver of its

252   progression (52) and adult acute respiratory distress syndrome (ARDS) is more often

253   associated with permanent alveolar simplification and fibrosis compared to infants or children

254   (53). This likely explains why children with ARDS experience less morbidity and mortality

255   outcomes compared to adults (54). An increase in ECM and collagen genes in the adult

256   macaques may be indicative of a dysregulation of injury repair. Targeting the ECM may be a

257   therapeutic strategy for promoting injury repair in adults with severe COVID-19.

258   Our study has limitations. Firstly, we only infected two dam-infant macaque pairs and

259   more animal numbers are needed to determine statistical differences. Additionally, a mock-

260   inoculated control group is necessary to decipher whether the differences observed are due to

261   SARS-CoV-2 infection alone, the age-dependent maturation of tissues and the immune

262   response, and/or experimental procedures. Finally, the time of euthanasia was not focused on

263   evaluating acute inflammatory responses in tissues, as at 2 weeks, virus replication is mainly

264   gone and tissue responses reflect repair in this animal model, and we evaluated trachea instead

265   of lung responses. However, our study is valuable in that it agrees with currently published data

266   in SARS-CoV-2-infected pediatric and adult cohorts and furthers our understanding of why

267   younger populations are less susceptible to severe COVID-19 compared to adults. Additionally,

268   this model will allow further definition of molecular mechanisms of age-dependent SARS-CoV-2

269   pathogenesis and assess efficacy of medical countermeasures.

270

271   **Methods**

272   **Animals, SARS-CoV-2 infection and sample collection.** The four Indian origin rhesus

273   macaques (Macaca mulatta) used in this study were housed at CNRPC in accordance with the

274   recommendations of the Association for Assessment and Accreditation of Laboratory Animal

275   Care International Standards and with the recommendations in the Guide for the Care and Use

276   of Laboratory Animals of the United States - National Institutes of Health. The Institutional

277   Animal Use and Care Committee approved these experiments (study protocol# 21702). All

278   animals were challenged through combined intratracheal (IT, 2.0 mL for dams, 1 ml for infants)

279   and intranasal (IN, 0.2 5 mL per nostril) inoculation with an infectious dose of 2.5 x 10^6 PFU for

280   the dams and 1.5 x 10^6 PFU for the infants of SARS-CoV-2 (2019-nCoV/USA-WA1/2020). The

281   stock was obtained from BEI Resources (NR-52281). The stock underwent deep sequencing to

282   confirm homology with the WA1/2020 isolate. Virus was stored at -80°C prior to use, thawed

283   rapidly at 37°C, and placed immediately on wet ice. Nasal swabs, pharyngeal swabs, BAL,

284   blood, breast milk and rectal swab samples were collected 1 week before infection and every 2-

285   3 days post-challenge. Nasopharyngeal, oropharyngeal and buccal secretions were collected

286   with FLOQSwabs™ (Copan), placed in a vial with DNA/RNA Shield™ solution (Zymo Research),

287   and stored at -70°C until further processing.

288   BAL was performed using a 20F rubber feeding tube with instillation of 20 ml sterile physiologic

289   saline followed by aspiration with a syringe. BAL samples were spun in the lab. The BAL cell

290   pellet, together with 0.5 ml of supernatant, was then mixed with 1.5 ml of TRIzol®-LS (Thermo

291   Fisher Scientific) and cryopreserved at -70° C. Additional aliquots of BAL supernatant were also

292   immediately cryopreserved. Blood and milk were collected and processed as previously

293   described (55-57).

294   Radiographs were obtained with a HF100+ Ultralight imaging unit (MinXRay, Northbrook, IL) at

295   50 kVp, 40mA, and 0.1 sec. Ventrodorsal, dorsoventral, R lateral, and L lateral radiographs

296   were obtained prior to inoculation and on days 1, 3, 5, 7, 10, and 14 post inoculation.

297   Radiographs were scored for the presence of pulmonary infiltrates by a board-certified

298   veterinary radiologist, who was blinded to the experimental group and time point, according to a

299   standard scoring system (0: normal; 1: mild interstitial pulmonary infiltrates; 2: moderate

300   pulmonary infiltrates perhaps with partial cardiac border effacement and small areas of

301   pulmonary consolidation; 3: severe interstitial infiltrates, large areas of pulmonary consolidation,

302   alveolar patterns and air bronchograms). Individual lobes were scored and scores per animal

303   per day were totaled.

304   At the end of the study, animals were euthanized, and a full necropsy was performed for tissue

305   collection, including trachea for cell isolation and fixed lung tissues for histopathology.

306   **Trachea collection and cell processing.** Upon necropsy, tracheobronchial tissues were

307   collected. Airway epithelial cells were isolated by placing tracheas in Minimum Essential

308   Medium Eagle; Joklik Modification (Lonza) containing 0.1% type XIV protease (Sigma-Aldrich),

309   50 U/mL penicillin, 50 µg/mL each streptomycin and gentamicin, and 100 µg/mL geneticin G418

310   (Invitrogen) overnight. Cells were gently aspirated off and stored in liquid nitrogen prior to RNA

311   isolation.

312   **Viral load assay**. SARS-CoV-2 infection was determined by quantitative Polymerase Chain

313   Reaction (qPCR) of SARS-CoV-2 Genomic (orf1a) and Subgenomic (N) RNA.

314   <u>SARS-CoV-2 Genomic (orf1a) qPCR</u>. A QIAsymphony SP (Qiagen, Hilden, Germany)

315   automated sample preparation platform along with a virus/pathogen DSP midi kit and the

316   complex800 protocol were used to extract viral RNA from 800 µL of respiratory sample. A

317   reverse primer specific to the orf1a sequence of SARS-CoV-2 (5'-

318   CGTGCCTACAGTACTCAGAATC-3') was annealed to the extracted RNA and then reverse

319   transcribed into cDNA using SuperScript™ III Reverse Transcriptase (Thermo Fisher Scientific,

320   Waltham, MA) along with RNAse Out (Thermo Fisher Scientific, Waltham, MA). The resulting

321   cDNA was then treated with Rnase H (Thermo Fisher Scientific, Waltham, MA) and added to a

322   custom 4x TaqMan™ Gene Expression Master Mix (Thermo Fisher Scientific, Waltham, MA)

323   containing primers and a fluorescently labeled hydrolysis probe specific for the orf1a sequence

324   of SARS-CoV-2 (forward primer 5'-GTGCTCATGGATGGCTCTATTA-3', reverse primer 5'-

325   CGTGCCTACAGTACTCAGAATC-3', probe 5'-/56-FAM/

326   ACCTACCTT/ZEN/GAAGGTTCTGTTAGAGTG GT/3IABkFQ/-3). All PCR setup steps were

327   performed using QIAgility instruments (Qiagen, Hilden, Germany). The qPCR was then carried

328   out on a QuantStudio 3 Real-Time PCR System (Thermo Fisher Scientific, Waltham, MA).

329   SARS-CoV-2 genomic (orf1a) RNA copies per reaction were interpolated using quantification

330   cycle data and a serial dilution of a highly characterized custom RNA transcript containing the

331   SARS-CoV-2 orf1a sequence. Mean RNA copies per milliliter were then calculated by applying

332   the assay dilution factor (DF=11.7). The limit of quantification (LOQ) for this assay is

333   approximately 31 RNA cp/mL (1.49 log10) with 800 uL of sample.

334   <u>Subgenomic (N) RNA qPCR assay</u>. A QIAsymphony SP (Qiagen, Hilden, Germany) automated

335   sample preparation platform along with a virus/pathogen DSP midi kit and the complex800

336   protocol were used to extract viral RNA from 800 µL of respiratory sample. The extracted RNA

337   was then added to TaqMan™ Fast Virus 1-Step Master Mix (Thermo Fisher Scientific, Waltham,

338   MA) containing primers and a fluorescently labeled hydrolysis probe specific for mRNA from the

339   nucleocapsid gene of SARS-CoV-2 (forward primer 5'-CGATCTCTTGTAGATCTGTTCTC-3',

340   reverse primer 5'-GGTGAACCAAGACGCAGTAT-3', probe 5'-/56-

341   FAM/TAACCAGAA/ZEN/TGGAGAACGCAGT GGG/3IABkFQ/-3'). All PCR setup steps were

342   performed using QIAgility instruments (Qiagen, Hilden, Germany). The qPCR was carried out

343   on a QuantStudio 3 Real-Time PCR System (Thermo Fisher Scientific, Waltham, MA). SARS-

344   CoV-2 subgenomic (N) RNA copies per reaction were interpolated using quantification cycle

345   data and a serial dilution of a highly characterized custom RNA transcript containing the SARS-

346   CoV-2 subgenomic nucleocapsid sequence. Mean RNA copies per milliliter were then

347   calculated by applying the assay dilution factor (DF=5.625). The limit of quantification (LOQ) for

348   this assay is approximately 31 RNA cp/mL (1.49 log10) with 800 uL of sample.

349   **Spike-specific IgG ELISA.**

350   IgG binding to the stabilized SARS-CoV-2 S protein S-2P was measured in plasma using ELISA

351   as previously described (58). Three hundred eighty-four–well plates were coated overnight with

352   S protein (2 µg/ml) produced by the Protein Production Facility (PPF) at the Duke Human

353 Vaccine Institute. Plates were then blocked with assay diluent (PBS containing 4% whey, 15%

354 normal goat serum, and 0.5% Tween 20). Ten serial fourfold dilutions starting at 1:10 for plasma

355 and undiluted for breast milk were added to the plates and incubated for 1 hour, followed by

356 detection with a horseradish peroxidase (HRP)–conjugated mouse anti-monkey IgG

357 (SouthernBiotech). The plates were developed by using an 2,2′-azinobis(3-

358 ethylbenzthiazolinesulfonic acid peroxidase substrate system (Colonial Scientific), and

359 absorbance was read at 450 nm with a SpectraMax microplate reader (Molecular Devices).

360 Results were calculated as AUC and EC_{50} values. AUC values were calculated using the

361 trapezoidal rule. EC_{50} values were calculated by fitting a four-parameter logistic function using

362 nonlinear regression. Pooled NHP convalescent serum to SARS-CoV-2 (BEI Resources, NR-

363 52401) was used in all IgG assays to ensure interassay reproducibility, but standard curves

364 were not developed given the lack of an SARS-CoV-2 RM-specific IgG reagent of known

365 concentration. IgA binding to S2P was measured following a similar ELISA protocol but using as

366 detection Ab anti-rhesus IgA 10F12-biotin (NHP Reagent Resource catalog AB_2819304)

367 followed by Streptadividin-HRP (Pierce, catalog 21126).

368 **Binding antibody multiplex assay**

369 SARS-CoV-2 antigens, including whole S (produced by PPF), S1 (Sino Biological, catalog no.

370 40591-V08H), S2 (Sino Biological, catalog no. 40590-V08B), RBD (Sino Biological, catalog no.

371 40592-V08H), and NTD (Sino Biological, catalog no. 40591-V49H) were conjugated to Magplex

372 beads (Bio-Rad, Hercules, CA). The conjugated beads were incubated on filter plates (Millipore,

373 Stafford, VA) for 30 min before plasma samples were added. Plasma samples were diluted in

374 assay diluent [1% dry milk, 5% goat serum, and 0.05% Tween 20 in PBS (pH 7.4.)] at a 1:1000-

375 point dilution. Beads and diluted samples were incubated for 30 min with gentle

376 rotation, and IgG binding was detected using a PE-conjugated mouse anti-monkey IgG

377 (SouthernBiotech, Birmingham, Alabama) at 2 µg/ml. Plates were washed and acquired on a

378 Bio-Plex 200 instrument (Bio-Rad, Hercules, CA), and IgG binding was reported as mean

379 fluorescence intensity (MFI). To assess assay background, the MFIs of wells without sample

380 (blank wells) were used, and nonspecific binding of the samples to unconjugated blank beads

381 was evaluated.

382 **Pseudovirus Ab neutralization assay**

383 SARS-CoV-2 neutralization was assessed with S-pseudotyped viruses in 293 T/ACE2 cells as a

384 function of reductions in luciferase (Luc) reporter activity. 293 T/ACE2 cells were provided by M.

385 Farzan and H. Mu at Scripps Florida. Cells were maintained in Dulbecco's modified Eagle's

386 medium containing 10% fetal bovine serum (FBS), 25 mM Hepes, gentamycin (50 μg/ml), and

387 puromycin (3 μg/ml). An expression plasmid encoding codon-optimized full-length S of the

388 Wuhan-1 strain (VRC7480) was provided by B.S.G. and K.S.C. at the Vaccine Research

389 Center, NIH (USA). The D614G amino acid change was introduced into VRC7480 by site-

390 directed mutagenesis using the QuikChange Lightning Site-Directed Mutagenesis Kit from

391 Agilent Technologies (catalog no. 210518). The mutation was confirmed by full-length S gene

392 sequencing. Pseudovirions were produced in HEK293 T/17 cells (American Type Culture

393 Collection, catalog no. CRL-11268) by transfection using Fugene 6 (Promega, catalog no.

394 E2692) and a combination of S plasmid, lentiviral backbone plasmid (pCMV ΔR8.2), and firefly

395 Luc reporter gene plasmid (pHR' CMV Luc) (78) in a 1:17:17 ratio. Transfections were allowed

396 to proceed for 16 to 20 hours at 37°C. Medium was removed, monolayers were rinsed with

397 growth medium, and 15 ml of fresh growth medium was added. Pseudovirus-containing culture

398 medium was collected after an additional 2 days of incubation and was clarified of cells by low-

399 speed centrifugation and 0.45-μm filtration and stored in aliquots at –80°C. Median tissue

400 culture infectious dose assays were performed on thawed aliquots to determine the infectious

401 dose for neutralization assays.

402 For neutralization, a pretitrated dose of pseudovirus was incubated with eight serial fivefold

403 dilutions of serum samples in duplicate in a total volume of 150 μl for 1 hour at 37°C in 96-well

404 flat-bottom poly-L-lysine–coated culture plates (Corning Biocoat). HEK 293T cells expressing

405   ACE2 receptors were suspended using TrypLE Select Enzyme solution (Thermo Fisher

406   Scientific) and immediately added to all wells (10,000 cells in 100 µl of growth medium per well).

407   One set of eight control wells received cells and virus (virus control), and another set of eight

408   wells received cells only (background control). After 66 to 72 hours of incubation, medium was

409   removed by gentle aspiration and 30 µl of Promega 1X lysis buffer was added to all wells. After

410   a 10-min incubation at RT, 100 µl of Bright-Glo Luc reagent was added to all wells. After 1 to 2

411   min, 110 µl of the cell lysate was transferred to a black/white plate (PerkinElmer). Luminescence

412   was measured using a PerkinElmer Life Sciences, Model Victor2 luminometer. Neutralization

413   titers are the serum dilution at which relative light units (RLUs) were reduced by either 50%

414   (ID_{50}) or 80% (ID_{80}) compared with virus control wells after subtraction of background RLUs.

415   Serum samples were heat-inactivated for 30 min at 56°C before assay.

416   **RNA isolation and transcript analysis**. Tracheal cells (epithelial, immune and mesenchymal)

417   were lysed in 350 ul of Trizol, and RNA was extracted by phenol:chloroform method, and

418   collected over RNAeasy column (Qiagen, Germantown, MD). The RNA concentration and

419   integrity was determined on the NanoDrop ND-1000 (Thermo Fisher Scientific). 1000ng RNA

420   from each sample was used as a template for preparing Illumina compatible libraries using the

421   TruSeq RNA Library Prep Kit v2 (Illumina). Library sizes were checked using D5000 high

422   sensitivity tape on the TapesSation 2200 (Agilent), and pooled libraries concentration were

423   determined by Qubit 3.0 Fluorometer (Thermo Fisher Scientific). A library input of 1.8 pM with

424   1% PhiX (Illumina) spike-in was sequenced using the NextSeq 500 instrument with the

425   NextSeq500/550 High Output v2.5 Kit (Illumina).

426   **Analysis of the bulk RNA-seq data.** RNA-Seq data was quality checked with FastQC (59) and

427   preprocessing was carried out using TrimGalore (60) toolkit to trim low-quality bases and

428   Illumina adapter sequences using default settings. Reads were aligned to the ENSEMBL

429   Homo_sapiens.GRCh38.dna.primary_assembly genome using the ENSEMBL

430   Homo_sapiens.GRCh38.100 transcript (61) annotation file with STAR (62) splice-aware RNA-

431   seq alignment tool in paired mode allowing maximum multimapping of 3. Gene level counts

432   were quantified using FeatureCounts (63) tool, counting unique features in non-stranded mode

433   and retaining both gene ID, gene name, and gene biotype mapping from the ENSEMBL

434   annotation file. Prior to differential expression analysis, count data was collapsed to donor level

435   and genes for which mean raw count was at least 15 were kept. Normalization and differential

436   expression were carried out with DESeq2 (64) Bioconductor (65) package, utilizing the 'apeglm'

437   Bioconductor package (66) for log fold change shrinkage, in R statistical programming

438   environment. The design formula was constructed to test for the effect of treatment while

439   controlling for donor.

440   The RNA-seq data was processed using the TrimGalore toolkit[1] which employs Cutadapt[2] to

441   trim low quality bases and Illumina sequencing adapters from the 3' end of the reads. Only

442   reads that were 20nt or longer after trimming were kept for further analysis. Reads were

443   mapped to the GRCh38v93 version of the human genome and transcriptome[3] using the STAR

444   RNA-seq alignment tool[4]. Reads were kept for subsequent analysis if they mapped to a single

445   genomic location. Gene counts were compiled using the HTSeq tool[5]. Only genes that had at

446   least 10 reads in any given library were used in subsequent analysis. Normalization and

447   differential expression was carried out using the DESeq2[6] Bioconductor[7] package with the R

448   statistical programming environment[8]. The false discovery rate was calculated to control for

449   multiple hypothesis testing. Gene set enrichment analysis[9] was performed to identify gene

450   ontology terms and pathways associated with altered gene expression for each of the

451   comparisons performed.

452   **Histopathology.** The lungs were harvested and each lobe separated. All lobes were

453   cannulated with 18-gauge blunt needles. All lobes were slowly infused with neutral buffered

454   formalin at 30 cm fluid pressure. Once fully inflated (approx. 30 mins) the main bronchus was

455   tied off and the lungs were placed in individual jars of formalin and fixed for 72 hours. Then they

456   were sliced from the hilus towards the periphery into slabs approximately 5mm thick. Each slab

457   was placed into a cassette recording its position in the stack and with further division of the slab

458   into smaller pieces if required to fit into the cassette. Tissues were then held in 70% ethanol

459   until processing and paraffin embedding followed by sectioning at 5 µm and generation of

460   hematoxylin and eosin (H&E) and Masson trichrome stained slides. Slides from every other slab

461   of the right and left caudal lobes were examined independently by 2 ACVP board certified

462   pathologists in a blinded manner.

463   **Immunohistochemistry (IHC).** Substance P (Thermo Fisher) and protein gene product 9.5

464   (Millipore Sigma) antibodies were applied to 5µm paraffin sections. The EnVision system

465   (Agilent) was used as the detection system with AEC (Agilent) as a chromogen. Paraffin

466   sections were treated in an antigen unmasking solution (Vector) at 100°C for 20 minutes before

467   incubation with a primary antibody. The slides were counterstained with Gill's hematoxylin

468   (StatLab). Primary antibodies were replaced by rabbit isotype control (Thermo Fisher) and run

469   with each staining series as the negative controls.

470   **Biocontainment and biosafety.** All work described here was performed with approved

471   standard operating procedures for SARS-CoV-2 in a biosafety level 3 (BSL-3) facility

472   conforming to requirements recommended in the Microbiological and Biomedical Laboratories,

473   by the U.S. Department of Health and Human Service, the U.S. Public Health Service, and the

474   U.S. Center for Disease Control and Prevention (CDC), and the National Institutes of Health

475   (NIH).

476

477 **Author contributions.**

478 S.N.L., C.G., C.P., T.T., T.D., Z.M., R.R., K.J.O., R.L.S., Y.S.L., J.W.R., J.W., J.U., R.I. and R.P.

479 performed experiments and analyzed the data, S.N.L. wrote the initial draft of the manuscript,

480 S.N.L., S.S.I., S.R.P., L.A.M., K.K.A.V.R. contributed to study design, data analysis and editing

481 of the manuscript. M.B. oversaw the planning and direction of the project including analysis and

482 interpretation of the data and editing of the manuscript. All authors edited the manuscript and

483 approved its final version.

488

References

1. Roser M RH. Coronavirus Disease (COVID-19). https://ourworldindata.org/coronavirus:.

2. Wu Z, and McGoogan JM. Characteristics of and Important Lessons From the Coronavirus Disease 2019 (COVID-19) Outbreak in China: Summary of a Report of 72 314 Cases From the Chinese Center for Disease Control and Prevention. *Jama.* 2020;323(13):1239-42.

3. Zhu N, Zhang D, Wang W, Li X, Yang B, Song J, et al. A Novel Coronavirus from Patients with Pneumonia in China, 2019. *N Engl J Med.* 2020;382(8):727-33.

4. Holshue ML, DeBolt C, Lindquist S, Lofy KH, Wiesman J, Bruce H, et al. First Case of 2019 Novel Coronavirus in the United States. *N Engl J Med.* 2020;382(10):929-36.

5. Denison MR. Severe acute respiratory syndrome coronavirus pathogenesis, disease and vaccines: an update. *Pediatr Infect Dis J.* 2004;23(11 Suppl):S207-14.

6. Assiri A, McGeer A, Perl TM, Price CS, Al Rabeeah AA, Cummings DA, et al. Hospital outbreak of Middle East respiratory syndrome coronavirus. *N Engl J Med.* 2013;369(5):407-16.

7. Khuri-Bulos N, Payne DC, Lu X, Erdman D, Wang L, Faouri S, et al. Middle East respiratory syndrome coronavirus not detected in children hospitalized with acute respiratory illness in Amman, Jordan, March 2010 to September 2012. *Clin Microbiol Infect.* 2014;20(7):678-82.

8. Donnelly CA, Ghani AC, Leung GM, Hedley AJ, Fraser C, Riley S, et al. Epidemiological determinants of spread of causal agent of severe acute respiratory syndrome in Hong Kong. *Lancet.* 2003;361(9371):1761-6.

9. Yang X, Yu Y, Xu J, Shu H, Xia J, Liu H, et al. Clinical course and outcomes of critically ill patients with SARS-CoV-2 pneumonia in Wuhan, China: a single-centered, retrospective, observational study. *Lancet Respir Med.* 2020.

10. Sheikh A, McMenamin J, Taylor B, Robertson C, Public Health S, and the EIIC. SARS-CoV-2 Delta VOC in Scotland: demographics, risk of hospital admission, and vaccine effectiveness. *Lancet.* 2021;397(10293):2461-2.

11. Chou J, Thomas PG, and Randolph AG. Immunology of SARS-CoV-2 infection in children. *Nature immunology.* 2022;23(2):177-85.

12. Loske J, Rohmel J, Lukassen S, Stricker S, Magalhaes VG, Liebig J, et al. Pre-activated antiviral innate immunity in the upper airways controls early SARS-CoV-2 infection in children. *Nat Biotechnol.* 2021.

13. Neeland MR, Bannister S, Clifford V, Dohle K, Mulholland K, Sutton P, et al. Innate cell profiles during the acute and convalescent phase of SARS-CoV-2 infection in children. *Nat Commun.* 2021;12(1):1084.

14. Sposito B, Broggi A, Pandolfi L, Crotta S, Clementi N, Ferrarese R, et al. The interferon landscape along the respiratory tract impacts the severity of COVID-19. *Cell.* 2021;184(19):4953-68 e16.

15. Chandrashekar A, Liu J, Martinot AJ, McMahan K, Mercado NB, Peter L, et al. SARS-CoV-2 infection protects against rechallenge in rhesus macaques. *Science.* 2020.

534 16. Williamson BN, Feldmann F, Schwarz B, Meade-White K, Porter DP, Schulz J, et
535   al. Clinical benefit of remdesivir in rhesus macaques infected with SARS-CoV-2.
536   *Nature.* 2020.
537 17. Van Rompay KKA, Olstad KJ, Sammak RL, Dutra J, Watanabe JK, Usachenko
538   JL, et al. Early treatment with a combination of two potent neutralizing antibodies
539   improves clinical outcomes and reduces virus replication and lung inflammation
540   in SARS-CoV-2 infected macaques. *PLoS pathogens.* 2021;17(7):e1009688.
541 18. Shaan Lakshmanappa Y, Elizaldi SR, Roh JW, Schmidt BA, Carroll TD, Weaver
542   KD, et al. SARS-CoV-2 induces robust germinal center CD4 T follicular helper
543   cell responses in rhesus macaques. *Nat Commun.* 2021;12(1):541.
544 19. Robinot R, Hubert M, de Melo GD, Lazarini F, Bruel T, Smith N, et al. SARS-
545   CoV-2 infection induces the dedifferentiation of multiciliated cells and impairs
546   mucociliary clearance. *Nat Commun.* 2021;12(1):4354.
547 20. Leal EC, Carvalho E, Tellechea A, Kafanas A, Tecilazich F, Kearney C, et al.
548   Substance P promotes wound healing in diabetes by modulating inflammation
549   and macrophage phenotype. *The American journal of pathology.*
550   2015;185(6):1638-48.
551 21. Liu H, Povysheva N, Rose ME, Mi Z, Banton JS, Li W, et al. Role of UCHL1 in
552   axonal injury and functional recovery after cerebral ischemia. 2019;116(10):4643-
553   50.
554 22. Weisberg SP, Connors TJ, Zhu Y, Baldwin MR, Lin WH, Wontakal S, et al.
555   Distinct antibody responses to SARS-CoV-2 in children and adults across the
556   COVID-19 clinical spectrum. *Nature immunology.* 2021;22(1):25-31.
557 23. Garrido C, Hurst JH, Lorang CG, Aquino JN, Rodriguez J, Pfeiffer TS, et al.
558   Asymptomatic or mild symptomatic SARS-CoV-2 infection elicits durable
559   neutralizing antibody responses in children and adolescents. *JCI insight.*
560   2021;6(17).
561 24. Yang HS, Costa V, Racine-Brzostek SE, Acker KP, Yee J, Chen Z, et al.
562   Association of Age With SARS-CoV-2 Antibody Response. *JAMA network open.*
563   2021;4(3):e214302.
564 25. Pierce CA, Preston-Hurlburt P, Dai Y, Aschner CB, Cheshenko N, Galen B, et al.
565   Immune responses to SARS-CoV-2 infection in hospitalized pediatric and adult
566   patients. *Sci Transl Med.* 2020;12(564):eabd5487.
567 26. Dowell AC, Butler MS, Jinks E, Tut G, Lancaster T, Sylla P, et al. Children
568   develop robust and sustained cross-reactive spike-specific immune responses to
569   SARS-CoV-2 infection. *Nature immunology.* 2022;23(1):40-9.
570 27. Muenchhoff M, Adland E, Karimanzira O, Crowther C, Pace M, Csala A, et al.
571   Nonprogressing HIV-infected children share fundamental immunological features
572   of nonpathogenic SIV infection. *Sci Transl Med.* 2016;8(358):358ra125.
573 28. Ditse Z, Muenchhoff M, Adland E, Jooste P, Goulder P, Moore PL, et al. HIV-1
574   Subtype C-Infected Children with Exceptional Neutralization Breadth Exhibit
575   Polyclonal Responses Targeting Known Epitopes. *Journal of virology.*
576   2018;92(17).
577 29. Goo L, Chohan V, Nduati R, and Overbaugh J. Early development of broadly
578   neutralizing antibodies in HIV-1-infected infants. *Nature medicine.*
579   2014;20(6):655-8.

580 30. Makhdoomi MA, Khan L, Kumar S, Aggarwal H, Singh R, Lodha R, et al.
581   Evolution of cross-neutralizing antibodies and mapping epitope specificity in
582   plasma of chronic HIV-1-infected antiretroviral therapy-naïve children from India.
583   *The Journal of general virology.* 2017;98(7):1879-91.
584 31. Mishra N, Sharma S, Dobhal A, Kumar S, Chawla H, Singh R, et al. Broadly
585   neutralizing plasma antibodies effective against autologous circulating viruses in
586   infants with multivariant HIV-1 infection. *Nat Commun.* 2020;11(1):4409.
587 32. Kumar S, Panda H, Makhdoomi MA, Mishra N, Safdari HA, Chawla H, et al. An
588   HIV-1 Broadly Neutralizing Antibody from a Clade C-Infected Pediatric Elite
589   Neutralizer Potently Neutralizes the Contemporaneous and Autologous Evolving
590   Viruses. *Journal of virology.* 2019;93(4).
591 33. Francis ME, Goncin U, Kroeker A, Swan C, Ralph R, Lu Y, et al. SARS-CoV-2
592   infection in the Syrian hamster model causes inflammation as well as type I
593   interferon dysregulation in both respiratory and non-respiratory tissues including
594   the heart and kidney. *PLoS pathogens.* 2021;17(7):e1009705.
595 34. Winkler ES, Bailey AL, Kafai NM, Nair S, McCune BT, Yu J, et al. SARS-CoV-2
596   infection of human ACE2-transgenic mice causes severe lung inflammation and
597   impaired function. *Nature immunology.* 2020;21(11):1327-35.
598 35. Munster VJ, Feldmann F, Williamson BN, van Doremalen N, Pérez-Pérez L,
599   Schulz J, et al. Respiratory disease in rhesus macaques inoculated with SARS-
600   CoV-2. *Nature.* 2020;585(7824):268-72.
601 36. Del Valle DM, Kim-Schulze S, Huang H-H, Beckmann ND, Nirenberg S, Wang B,
602   et al. An inflammatory cytokine signature predicts COVID-19 severity and
603   survival. *Nature medicine.* 2020;26(10):1636-43.
604 37. Zhao Y, Qin L, Zhang P, Li K, Liang L, Sun J, et al. Longitudinal COVID-19
605   profiling associates IL-1RA and IL-10 with disease severity and RANTES with
606   mild disease. *JCI insight.* 2020;5(13).
607 38. Cheemarla NR, Watkins TA, Mihaylova VT, Wang B, Zhao D, Wang G, et al.
608   Dynamic innate immune response determines susceptibility to SARS-CoV-2
609   infection and early replication kinetics. *The Journal of experimental medicine.*
610   2021;218(8).
611 39. Ince LM, Weber J, and Scheiermann C. Control of Leukocyte Trafficking by
612   Stress-Associated Hormones. 2019;9.
613 40. Yoshida M, Worlock KB, Huang N, Lindeboom RGH, Butler CR, Kumasaka N, et
614   al. Local and systemic responses to SARS-CoV-2 infection in children and
615   adults. *Nature.* 2021.
616 41. Loske J, Röhmel J, Lukassen S, Stricker S, Magalhães VG, Liebig J, et al. Pre-
617   activated antiviral innate immunity in the upper airways controls early SARS-
618   CoV-2 infection in children. *Nature Biotechnology.* 2021.
619 42. Netea MG, Domínguez-Andrés J, Barreiro LB, Chavakis T, Divangahi M, Fuchs
620   E, et al. Defining trained immunity and its role in health and disease. *Nature
621   Reviews Immunology.* 2020;20(6):375-88.
622 43. Elahi S. Neonatal and Children's Immune System and COVID-19: Biased
623   Immune Tolerance versus Resistance Strategy. 2020;205(8):1990-7.
624 44. Midulla F, Cristiani L, and Mancino E. Will children reveal their secret? The
625   coronavirus dilemma. *The European respiratory journal.* 2020;55(6).

45. Alvira CM, Abate A, Yang G, Dennery PA, and Rabinovitch M. Nuclear factor-kappaB activation in neonatal mouse lung protects against lipopolysaccharide-induced inflammation. *American journal of respiratory and critical care medicine.* 2007;175(8):805-15.

46. Yang G, Abate A, George AG, Weng YH, and Dennery PA. Maturational differences in lung NF-kappaB activation and their role in tolerance to hyperoxia. *The Journal of clinical investigation.* 2004;114(5):669-78.

47. Ying L, Alvira CM, and Cornfield DN. Developmental differences in focal adhesion kinase expression modulate pulmonary endothelial barrier function in response to inflammation. *American journal of physiology Lung cellular and molecular physiology.* 2018;315(1):L66-I77.

48. Hellman U, Karlsson MG, Engström-Laurent A, Cajander S, Dorofte L, Ahlm C, et al. Presence of hyaluronan in lung alveoli in severe Covid-19: An opening for new treatment options? *The Journal of biological chemistry.* 2020;295(45):15418-22.

49. Wool GD, and Miller JL. The Impact of COVID-19 Disease on Platelets and Coagulation. *Pathobiology : journal of immunopathology, molecular and cellular biology.* 2021;88(1):15-27.

50. Wendisch D, Dietrich O, Mari T, von Stillfried S, Ibarra IL, Mittermaier M, et al. SARS-CoV-2 infection triggers profibrotic macrophage responses and lung fibrosis. *Cell.* 2021;184(26):6243-61.e27.

51. Boyd DF, Allen EK, Randolph AG, Guo X-zJ, Weng Y, Sanders CJ, et al. Exuberant fibroblast activity compromises lung function via ADAMTS4. *Nature.* 2020;587(7834):466-71.

52. Herrera J, Henke CA, and Bitterman PB. Extracellular matrix as a driver of progressive fibrosis. *The Journal of clinical investigation.* 2018;128(1):45-53.

53. Im D, Shi W, and Driscoll B. Pediatric Acute Respiratory Distress Syndrome: Fibrosis versus Repair. *Front Pediatr.* 2016;4:28-.

54. Orloff KE, Turner DA, and Rehder KJ. The Current State of Pediatric Acute Respiratory Distress Syndrome. *Pediatric allergy, immunology, and pulmonology.* 2019;32(2):35-44.

55. Permar SR, Wilks AB, Ehlinger EP, Kang HH, Mahlokozera T, Coffey RT, et al. Limited contribution of mucosal IgA to Simian immunodeficiency virus (SIV)-specific neutralizing antibody response and virus envelope evolution in breast milk of SIV-infected, lactating rhesus monkeys. *Journal of virology.* 2010;84(16):8209-18.

56. Jensen K, Nabi R, Van Rompay KKA, Robichaux S, Lifson JD, Piatak M, Jr., et al. Vaccine-Elicited Mucosal and Systemic Antibody Responses Are Associated with Reduced Simian Immunodeficiency Viremia in Infant Rhesus Macaques. *Journal of virology.* 2016;90(16):7285-302.

57. Marthas ML, Van Rompay KK, Abbott Z, Earl P, Buonocore-Buzzelli L, Moss B, et al. Partial efficacy of a VSV-SIV/MVA-SIV vaccine regimen against oral SIV challenge in infant macaques. *Vaccine.* 2011;29(17):3124-37.

58. Dennis M, Eudailey J, Pollara J, McMillan AS, Cronin KD, Saha PT, et al. Coadministration of CH31 Broadly Neutralizing Antibody Does Not Affect

Development of Vaccine-Induced Anti-HIV-1 Envelope Antibody Responses in Infant Rhesus Macaques. *Journal of virology.* 2019;93(5).

59. Andrews S. FastQC: a quality control tool for high throughput sequence data. . http://www.bioinformatics.babraham.ac.uk/projects/fastqc/.

60. Krueger F. A wrapper tool around Cutadapt and FastQC to consistently apply quality and adapter trimming to FastQ files, with some extra functionality for MspI-digested RRBS-type (Reduced Representation Bisufite-Seq) libraries. http://www.bioinformatics.babraham.ac.uk/projects/trim_galore/.

61. Kersey PJ, Staines DM, Lawson D, Kulesha E, Derwent P, Humphrey JC, et al. Ensembl Genomes: an integrative resource for genome-scale data from non-vertebrate species. *Nucleic Acids Res.* 2012;40(Database issue):D91-7.

62. Dobin A, Davis CA, Schlesinger F, Drenkow J, Zaleski C, Jha S, et al. STAR: ultrafast universal RNA-seq aligner. *Bioinformatics.* 2013;29(1):15-21.

63. Liao Y, Smyth GK, and Shi W. featureCounts: an efficient general purpose program for assigning sequence reads to genomic features. *Bioinformatics.* 2014;30(7):923-30.

64. Love MI, Huber W, and Anders S. Moderated estimation of fold change and dispersion for RNA-seq data with DESeq2. *Genome Biol.* 2014;15(12):550.

65. Huber W, Carey VJ, Gentleman R, Anders S, Carlson M, Carvalho BS, et al. Orchestrating high-throughput genomic analysis with Bioconductor. *Nat Methods.* 2015;12(2):115-21.

66. Zhu A, Ibrahim JG, and Love MI. Heavy-tailed prior distributions for sequence count data: removing the noise and preserving large differences. *Bioinformatics.* 2019;35(12):2084-92.
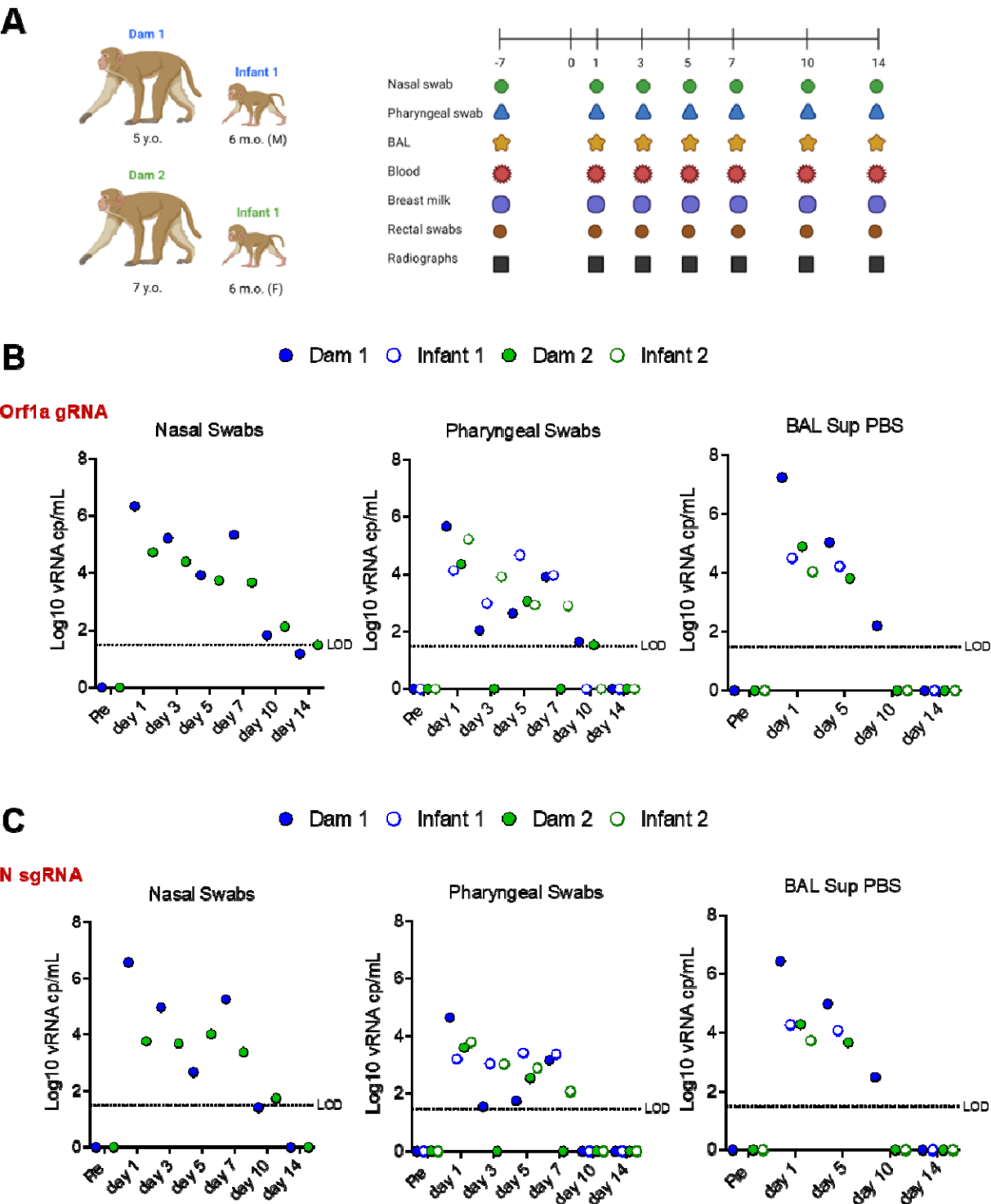
697

698

699

700

701 Fig. 1

702 **Experimental design and SARS-CoV-2 RNA shedding**

703 **A** Two dams and their 6-month-old infants were inoculated intratracheally and intranasally with

704 2.5 x 10^6 PFU and 1.5 x 10^6 PFU of SARS-CoV-2 (WA strain), respectively. Nasal and

705 pharyngeal swabs, bronchoalveolar lavage (BAL), blood, breast milk and rectal swabs were

706 collected over time up to day 14 post-challenge. Additionally, lung radiographs were performed

707 throughout the experiment. **B** Log_{10} viral RNA copies per mL are reported for nasal swabs,

708 pharyngeal swabs and BAL supernatants over time for both the genomic (Orf1a gene) and **C**
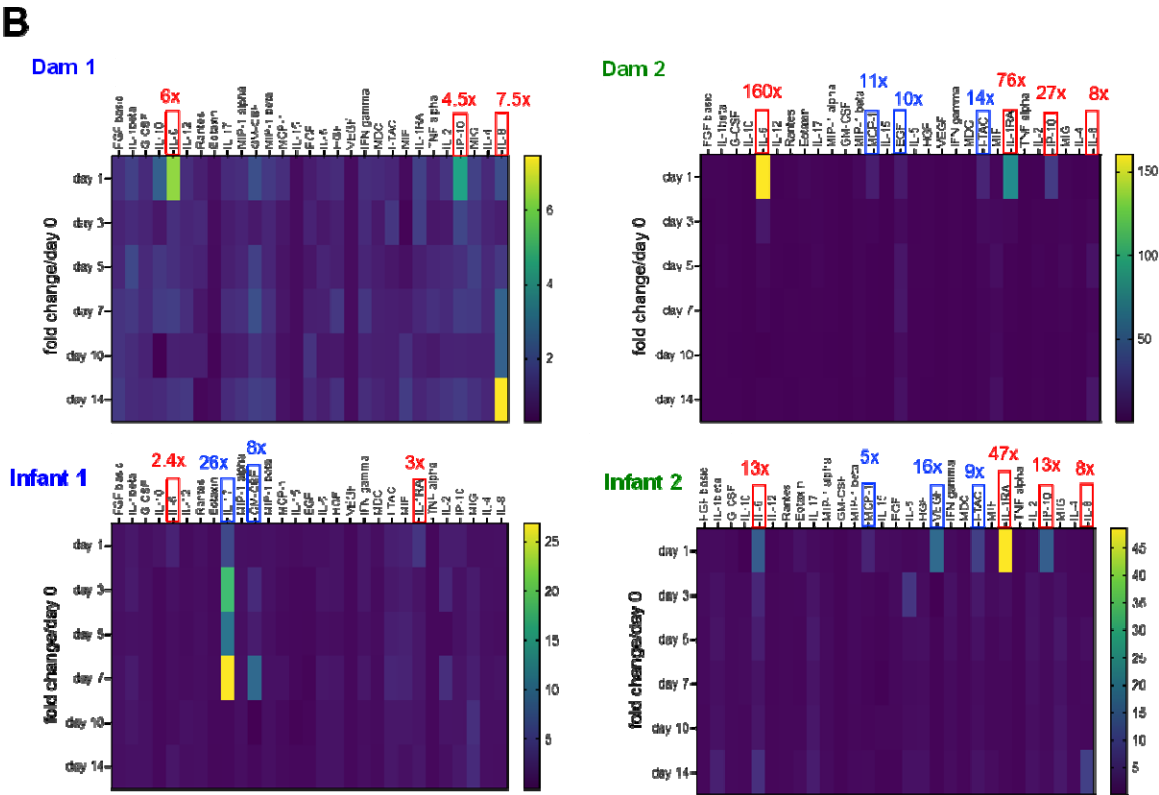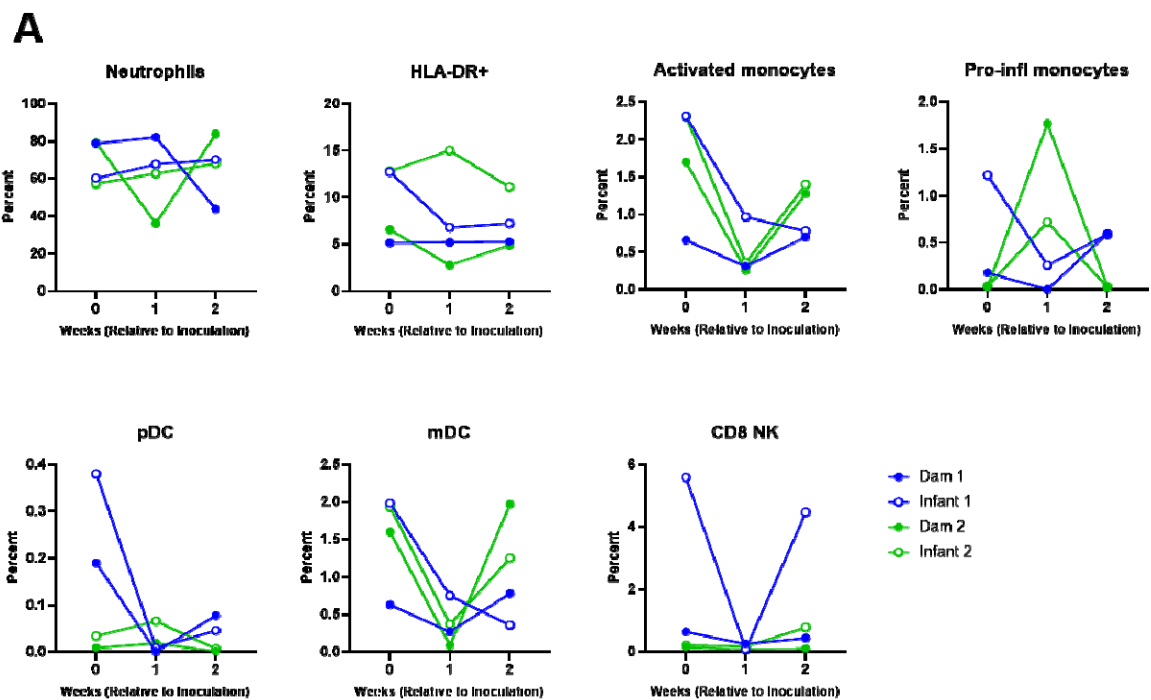
709 subgenomic (N gene) viral RNA.

710

711

712

713

714   Fig. 2

715   **Circulating innate immune cell and cytokine responses in SARS-CoV-2-infected dam and**

716   **infant rhesus macaques**

717   **A** Kinetics of innate immune cell responses including neutrophils, total HLA-DR+ (lineage-,

718   CD66-) cells, activated monocytes, pro-inflammatory monocytes, plasmacytoid dendritic cells

719   (pDC), myeloid dendritic cells (mDC) and CD8$^+$ natural killer (NK) cells. **B** Heat maps of innate

720   cytokines for each animal represented as fold change over day 0 post SARS-CoV-2 infection.

721   Notable increases in key cytokines are denoted in red box (values in red represent peak fold

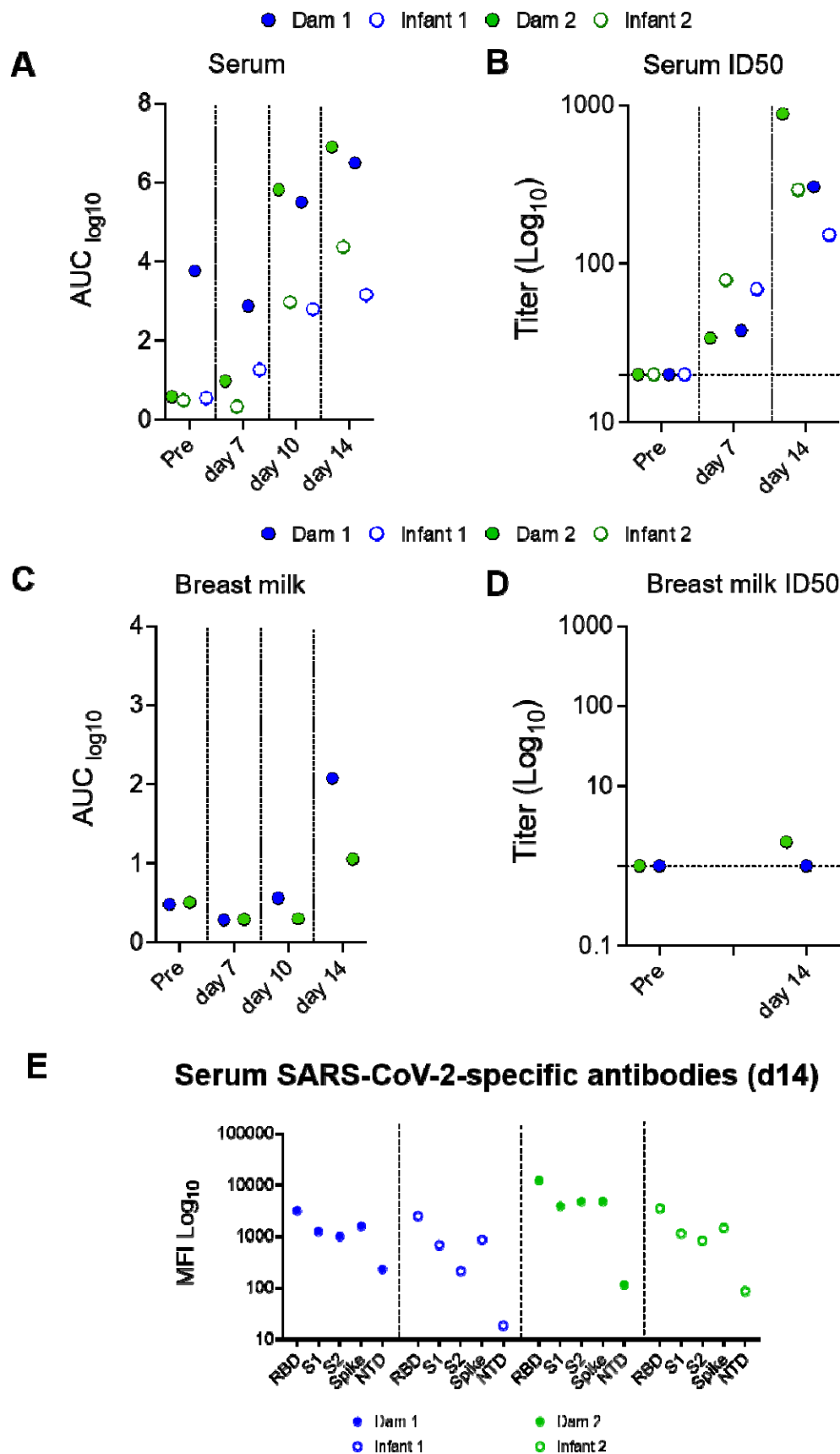722   change over day 0). The scale to the right of the heat map is in pg/ml.

723

725 Fig. 3

726 **SARS-CoV-2-elicited binding and neutralizing antibody (nAb) responses in infant and**

727 **dam rhesus macaques**

728 **A** S-2P protein-specific antibody responses were measured in serum and **C** breast milk by

729 ELISA. Serial dilutions of plasma (starting at 1:10) and breast milk (starting at 1:1) were

730 assayed for IgG binding to SARS-CoV-2 S. Data are reported as $\log_{10}$ AUC values. **B**

731 Neutralization capacity in serum and **D** breast milk was measured using S D614G-pseudotyped

732 viruses and HEK 293T cells expressing ACE2 receptors**.** Results are expressed as reciprocal

733 50% inhibitory dilution (ID$_{50}$). Gray dotted lines represent detection cutoff. **E** Antibody epitope

734 specificity measured by binding antibody multiplex assay (BAMA). Plasma was diluted 1:1,000

735 to measure binding to different domains of the S protein, including the RBD, S1, S2, full-length

736 S protein, and NTD. Binding antibody responses are reported as $\log_{10}$-transformed MFI after

737 subtraction of background values.
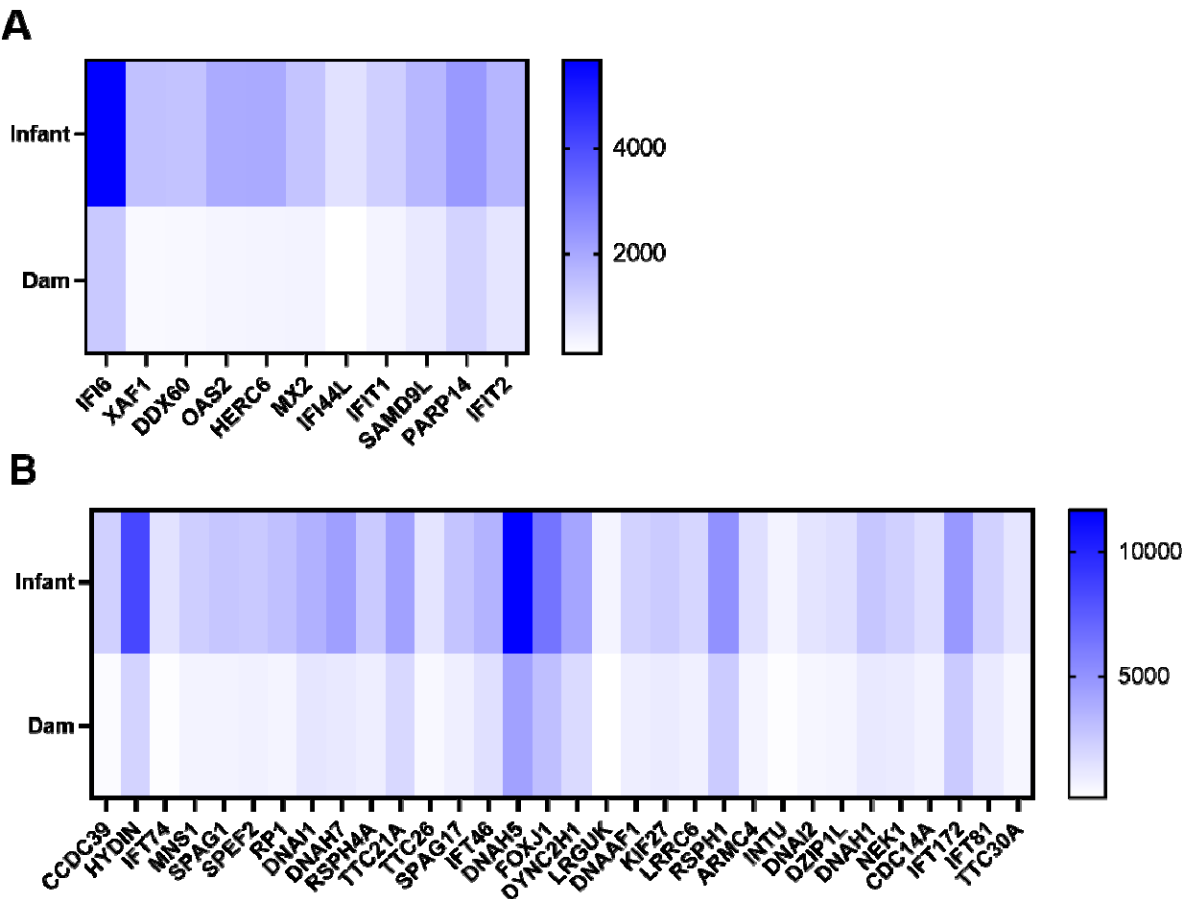
738

739

740
741   Fig. 4

742   **Age-dependent differences in transcriptomic responses in the trachea reveal**

743   **downregulated interferon stimulated genes and cilia injury signatures in adult macaques**

744   **A** Heat map of differentially expressed interferon stimulated genes and **B** genes related to cilia

745   structure and function that are downregulated in adult compared with infant macaques 14 days

746   after SARS-CoV-2 infection. Blue represents relative upregulation of gene expression and white

747   represents relative downregulation of gene expression. Genes are arranged by $\log_2$ fold change

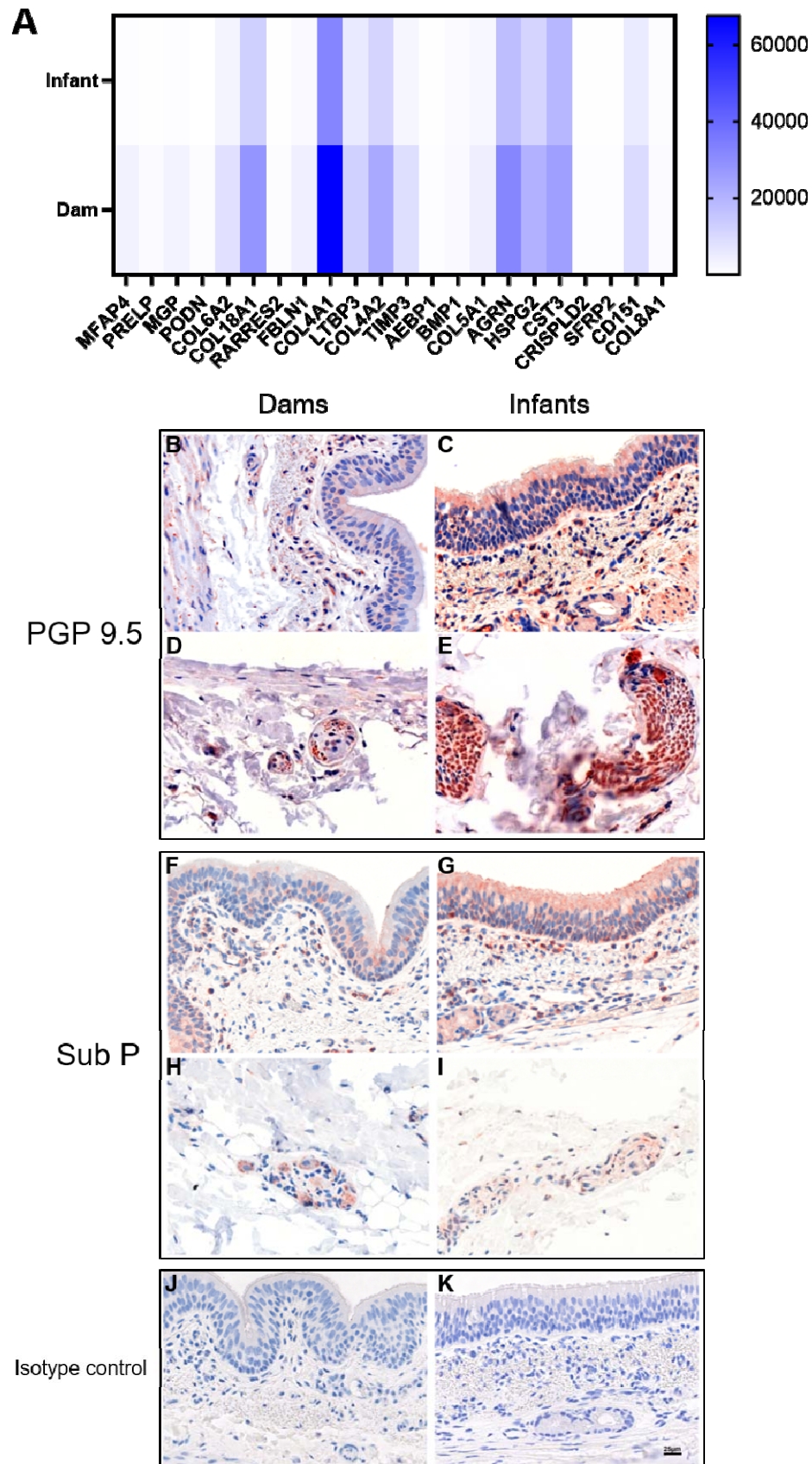748   with the largest $\log_2$ fold change to the left and the smallest $\log_2$ fold change to the right.

749

750

751

752   Fig. 5

753   **Upper airways of SARS-CoV-2 infected adult macaques have a profibrotic transcriptomic**

754   **signature**

755   **A** Heat map of differentially expressed genes related to extracellular matrix structure and

756   metabolism that are upregulated in adult compared with infant macaques 14 days after SARS-

757   CoV-2 infection. Blue represents relative upregulation of gene expression and white represents

758   relative downregulation of gene expression. Genes are arranged by log_2 fold change with the

759   largest log_2 fold change to the left and the smallest log_2 fold change to the right. Assessment of

760   protein gene product (PGP) 9.5 expression in (**B**) dam 1, (**D**) dam 2, (**E**) infant 1 and (**C**) infant

761   2, substance P (sub P) expression in (**F**) dam 1, (**H**) dam 2, (**I**) infant 1 and (**G**) infant 2 trachea

762   tissues and (**J**) dam and (**K**) infant isotype controls via immunohistochemical staining.

763